

Atomic Engineering Bifunctional Niobium (V)-based Heterostructure Nanosheet for High Efficiency Lean-Electrolyte Lithium-Sulfur Full Batteries

Haodong Shi

Dalian Institute of Chemical Physics, Chinese Academy of Sciences

Jieqiong Qin

Dalian Institute of Chemical Physics

Pengfei Lu

Dalian Institute of Chemical Physics

Cong Dong

Dalian Institute of Chemical Physics

Prattek Das

Dalian Institute of Chemical Physics

Jiemin Wang

Dalian Institute of Chemical Physics, Chinese Academy of Sciences

Liangzhu Zhang

Dalian Institute of Chemical Physics, Chinese Academy of Sciences

Zhong-Shuai Wu (✉ wuzs@dicp.ac.cn)

Dalian Institute of Chemical Physics, Chinese Academy of Sciences <https://orcid.org/0000-0003-1851-4803>

Article

Keywords: high-efficiency lithium-sulfur (Li-S) batteries, batteries, electrocatalysis, energy transfer

Posted Date: January 29th, 2021

DOI: <https://doi.org/10.21203/rs.3.rs-150414/v1>

License: © ⓘ This work is licensed under a Creative Commons Attribution 4.0 International License.

[Read Full License](#)

Abstract

High-efficiency lithium-sulfur (Li-S) batteries depend on advanced electrode structure that can attain high sulfur utilization at lean-electrolyte and limited lithium. Herein, a twinborn holey $\text{Nb}_4\text{N}_5\text{-Nb}_2\text{O}_5$ heterostructure is designed as a dual-functional host for both redox-kinetics-accelerated sulfur cathode and dendrite-inhibited Li anode simultaneously for long-cycling and lean-electrolyte Li-S full batteries. Benefiting from the accelerative polysulfides anchoring-diffusion converting efficiency and electronic-conducting properties of $\text{Nb}_4\text{N}_5\text{-Nb}_2\text{O}_5$, polysulfide-shutting is significantly alleviated. Meanwhile, the lithiophilic nature of holey $\text{Nb}_4\text{N}_5\text{-Nb}_2\text{O}_5$ is applied as ion-redistributor for homogeneous Li-ion deposition. Taking advantage of these merits, the Li-S full batteries present the excellent electrochemical properties, including a minimum capacity decay of 0.025% per cycle, and a high areal-capacity of 5.0 mAh cm^{-2} at sulfur loading of 6.9 mg cm^{-2} , corresponding to negative to positive capacity ratio (2.4:1) and electrolyte to sulfur ratio ($5.1 \text{ } \mu\text{L mg}^{-1}$). Therefore, this work opens a new avenue for boosting high-performances Li-S batteries towards practical applications.

Introduction

The growing demands for both hand-held electronics and electric vehicles have promoted the exploration of high-energy-density rechargeable batteries over 400 Wh kg^{-1} . Lithium-sulfur (Li-S) batteries with exceptional theoretical energy density ($\sim 2500 \text{ Wh kg}^{-1}$), coupled with highly reversible and efficient reactions at the sulfur cathode-electrolyte interface (solid sulfur-soluble lithium polysulfides-insoluble Li_2S) and lithium (Li) anode-electrolyte (lithium striping-plating) are one of the most appealing battery techniques². Basically, the physicochemical properties of the designed electrode host materials significantly influence the reversibility and kinetics of the heterogeneous reaction of Li-S batteries. In addition, the capacity degradations resulting from the irreversible lithium polysulfides (LiPSs) "shuttle effect" on the sulfur cathode, and safety concern deriving from huge volume change and uncontrollable dendrite-forming on the Li metal anode, have severely impeded the commercial generalization³. In this regard, a low electrolyte-to-sulfur (E/S) ratio ($< 6 \text{ } \mu\text{L mg}^{-1}$) and low negative to positive (N/P) capacity ratio (< 5) under high sulfur loading ($> 5 \text{ mg cm}^{-2}$) are required for practical Li-S batteries⁴.

For the cathode, intensive efforts have been devoted to effectively confine the original sulfur particles, soluble polysulfides and final solid discharged products via physical and chemical immobilization. The polar materials, especially with catalytic effect, such as metal oxides⁵, sulfides⁶, phosphides⁷, nitrides⁸ and functional carbons⁹, have shown improved electrical performance of sulfur electrodes by enhancing the reaction kinetics and chemical conversion of LiPSs¹⁰. Although with great progress, implementing high electrical conductivity, strong adsorption and abundant catalytic sites simultaneously from a single electrode remains challenging¹¹. Recently, constructing heterostructure sulfur host by the surface and interface engineering presents the most ideal route to achieve LiPSs chemical adsorption, promote electron and charge transfer at interfaces and improve their surface redox kinetics LiPSs regulation¹².

Apart from sulfur cathode, various strategies have been explored for modifying the Li metal anodes since the fully assembled Li-S batteries strongly depend on the synergy between sulfur and Li electrodes. For instance, they include the engineering of artificial protection layers¹³, optimizing the electrolytes with additives¹⁴, using high-surface-area 3D conductive scaffolds¹⁵, and developing solid-state or polymer electrolytes¹⁶. However, the inhomogeneous Li ion flux distribution and mass transfers, especially at high current density still emerge during the repeated Li plating and stripping process, which could not fully prohibit the formation of Li dendrites and dead Li¹⁷. In addition, a lithiophilic matrix led to a certain threshold of Li deposition on the lithiophilic surface, hence resulting in the growth of dendrites^{18, 19, 20, 21}. To overcome this issue, nanoporous structures such as vertical microchannels²², aligned holey nanosheets¹⁷ and 3D structure containing nanopore²³ serving as ion redistributors have been proposed to homogenize Li-ion flux on the electrolyte-electrode interface for dendrite-free Li anodes. In short, rational construction of a lithiophilic heterostructured material integrating precise nanoporous surface and interface engineering for both sulfur host and Li metal anode is promising for boosting the performance of Li-S batteries.

Herein, we designed a holey 2D Nb₄N₅-Nb₂O₅ heterostructure as a dual-functional host material for both sulfur cathode (Nb₄N₅-Nb₂O₅/S) and Li anode (Nb₄N₅-Nb₂O₅/Li). Such a bibasic host integrated strong chemisorptive Nb₂O₅ and high conductive Nb₄N₅, simultaneously facilitating high trapping efficiency and fast electron transportation of LiPSs conversion on the heterostructure surface. As for the anode scaffold, the holey lithiophilic Nb₄N₅-Nb₂O₅ heterostructure greatly reduced the deposition current density and enabled homogeneous Li-ion distribution, hence suppressing Li dendrite formation. Based on that, a meticulously designed Li-S full battery configuration was achieved with super-rate capability of 1163 mAh g⁻¹ at 3 C and remarkable cycle stability over 1000 cycles (capacity degradation rate of 0.025% per cycle). Furthermore, a promising areal capacity up to 5.0 mAh cm⁻² for 200 cycles with a high sulfur loading (6.9 mg cm⁻²) was achieved for the Nb₄N₅-Nb₂O₅/Li||Nb₄N₅-Nb₂O₅/S batteries. Thus, this work presents a novel design of advanced host to comprehensively address the obstacles in sulfur cathode and Li anode towards the high-performance Li-S batteries.

Results

Fabrication and Characterization of Nb₄N₅-Nb₂O₅ Heterostructure. The desirable properties of electrocatalysts for fast conversion of LiPSs are dominated by three main factors: (a) high adsorption ability to anchor LiPSs, (b) rich catalytic active sites to enhance the conversion kinetics, and (c) good electrical conductivity for effectively electron transfer^{24, 25}. Based on that, 2D Nb₄N₅-Nb₂O₅ heterostructure integrates those properties with synergetic effect of Nb₂O₅ and Nb₄N₅. To be more specific, the bare Nb₂O₅ possesses desirable chemical adsorption, which is necessary for the LiPSs. However, electrical conductivity is not high for electrons transfer²⁶. In contrast, polar Nb₄N₅ with superior electrical conductivity facilitates efficient conversion of LiPSs, but poor affinity of the LiPSs on its surface²⁷. Therefore, the novel design of Nb₄N₅-Nb₂O₅ heterostructure by coupling the merits of highly

adsorptive Nb_2O_5 and conductive Nb_4N_5 can enable a fast nucleation and conversion of the LiPSs. Consequently, the LiPSs shuttling is effectively confined and the utilization of sulfur is greatly promoted (Fig. 1a).

The 2D Nb_4N_5 - Nb_2O_5 heterostructures were prepared by a facile hydrothermal and subsequent ammonia annealing treatment. The scanning electron microscope (SEM) image showed uniform flower morphology, composed of holey nanosheets (Fig. 1b and Supplementary Fig. 1). Significantly, the composition of Nb_4N_5 - Nb_2O_5 heterostructure could be adjusted by nitriding temperature and time. As a result, Nb_2O_5 - Nb_4N_5 heterostructures with the ratio of around 1:1 (Supplementary Table 1) were successfully obtained (Fig. 1c). The high-resolution transmission electron microscope (TEM) images illustrated that the lattice spacings were 0.25 nm and 0.39 nm, matching the (211) planes of Nb_4N_5 (Supplementary Fig. 2) and (001) planes of Nb_2O_5 (Supplementary Fig. 3), respectively. More importantly, a heterostructured interface between them was clearly observed (Fig. 1d). Such an interface was not only conducive for fast electron transportation, but also improved the adsorption and conversion of LiPSs²⁴. In addition, the porous structure was beneficial to offer easy accessibility to LiPSs with rich active sites for the consequent adsorption and catalytic conversion (Fig. 1e and Supplementary Fig. 4). X-ray photoelectron spectroscopy (XPS) further confirmed the existence of Nb-O, Nb-N bonding configuration (Fig. 1f)²⁸. The intact connection and uniform distribution of Nb_2O_5 and Nb_4N_5 were verified by the energy-dispersive spectrometry element mapping results (Fig. 1g).

Electrocatalytic and Adsorption Effects of Nb_4N_5 - Nb_2O_5 Heterostructure. First-principle calculations were performed to disclose the chemical interaction of LiPSs (Li_2S_4 was chosen as the prototype for modelling) with Nb_2O_5 and Nb_4N_5 configurations. The adsorption energies of Li_2S_4 on Nb_4N_5 (211) and Nb_2O_5 (001) surfaces were - 4.8 eV and - 6.2 eV respectively, indicating that Nb_2O_5 had higher adsorption affinity for LiPSs²⁹. Further, the superior conductivity of Nb_4N_5 guaranteed the fast diffusion of LiPSs from Nb_2O_5 surface to Nb_4N_5 surface across the interfacial migration between them (Fig. 2a, b). As a result, Nb_4N_5 - Nb_2O_5 could efficiently enhance the electrochemical reactions and accelerate the oxidation conversion of dissolved LiPSs to solid Li_2S in the discharge process, which ensured a discharging/charging loop process with excellent reversibility (Fig. 2c).

We selected the Nb_4N_5 - Nb_2O_5 heterostructure (with the ratio of around 1:1) as the model catalyst representation for deducing the reaction mechanism of electrocatalysis in corresponding Li-S batteries. Nb_4N_5 - Nb_2O_5 mixture (Nb_4N_5 - Nb_2O_5 mix with the ratio of 1:1), bare Nb_4N_5 and bare Nb_2O_5 were also selected for comparison. In order to confirm the improved redox-reaction kinetics in the liquid-liquid transformation process, cyclic voltammetry (CV) measurement using symmetric batteries based on Li_2S_6 catholyte were employed. The redox current response increased in the order of $\text{Nb}_2\text{O}_5 < \text{Nb}_4\text{N}_5 < \text{Nb}_4\text{N}_5$ - Nb_2O_5 mix $< \text{Nb}_4\text{N}_5$ - Nb_2O_5 heterostructure (Fig. 2d), reflecting that Nb_4N_5 - Nb_2O_5 heterostructure possessed better interfacial kinetics³⁰. Apart from the liquid-liquid transformation of LiPSs, the polar and conductive heterostructure also played a key role at liquid-solid boundary. A potentiostatic nucleation

experiment was conducted to understand the electrochemical deposition from LiPSs to solid Li₂S. Specifically, the capacity 168 mAh g⁻¹ of the precipitated Li₂S on Nb₄N₅-Nb₂O₅ heterostructure electrode was much higher than those of Nb₄N₅-Nb₂O₅ mix (132 mAh g⁻¹), Nb₄N₅ (124 mAh g⁻¹), and Nb₂O₅ (88 mAh g⁻¹). Besides, the battery with Nb₄N₅-Nb₂O₅ heterostructure exhibited the highest current density of 0.074 mA, suggesting the role of heterostructure in fast LiPSs trapping and nucleation of Li₂S (Fig. 2e-h)³¹. Moreover, the sluggish oxidation kinetics of solid Li₂S at the charging cycle is the dominant factor for the reduced reversibility of Li₂S-to-LiPSs interconversion, thus leaving behind unusable electrochemical phases (also called “dead sulfur”). Similarly, kinetic evaluation of Li₂S decomposition was conducted by a potentiostatic charging process after full discharge into solid Li₂S. Nb₄N₅-Nb₂O₅ heterostructure showed an obvious oxidation current peak at 577 s, which was much earlier than those of Nb₄N₅-Nb₂O₅ mix (763 s), Nb₄N₅ (1021 s) and Nb₂O₅ (2620 s). In addition, the improved Li₂S dissolution could reduce the deactivation of the catalyst surface and increase the utilization of sulfur³². Furthermore, the linear sweep voltammetry (LSV) indicated that Nb₄N₅-Nb₂O₅ heterostructure electrode exhibited highest reaction peak current (0.43 mA cm⁻²) with lowest Tafel slope (89.4 mV dec⁻¹), further demonstrative of the improved kinetics of LiPSs redox reactions (Fig. 2j and Supplementary Fig. 5)³³.

To study the chemical adsorption behavior of the Nb₄N₅-Nb₂O₅ heterostructure for LiPSs, a visual adsorption test was conducted by adding the same amount (~ 5 mg) of materials into the Li₂S₆ solution. As shown in Fig. 2k, the solution with Nb₄N₅-Nb₂O₅ heterostructure additive rapidly decolorized. The sample with Nb₂O₅ showed slightly inferior decoloration phenomenon compared to the heterostructure due to the limited specific area (33.9 m² g⁻¹) than that of heterostructure (40.5 m² g⁻¹), while the control sample with bare Nb₄N₅ showed minor difference (Fig. 1e and Supplementary Fig. 4). This was consistent with the ultraviolet-visible (UV-vis) absorption and density functional theory (DFT) calculation results. Moreover, the nature of the interaction between LiPSs and Nb₄N₅-Nb₂O₅ heterostructure was probed by XPS measurement. In the deconvoluted Li 1s spectrum, two obvious peaks at 60.9 eV and 59.7 eV were observed, corresponding to Li-O and Li-N bond (Fig. 2l). Moreover, additional Nb-S peaks (203.7 eV, 206.3 eV) were detected in Nb 3d XPS spectrum³⁴. These results indicated that the Nb₄N₅-Nb₂O₅ heterostructure strongly interacted with LiPSs (Fig. 2m), offering a potential functional material for LiPSs electrocatalysis.

To demonstrate the favorable LiPSs adsorption and electrocatalytic reactivity of Nb₄N₅-Nb₂O₅ heterostructure on the sulfur reactions, the half-cell configurations were fabricated with a Li metal foil as anode and Nb₄N₅-Nb₂O₅ heterostructure, Nb₄N₅-Nb₂O₅ mix, Nb₄N₅ and Nb₂O₅ loaded with sulfur as cathodes respectively to evaluate their electrochemical performance. The CV curves of all the assembled Li-S batteries showed the typical pair of redox peaks, corresponding to the formation of soluble LiPSs (2.2–2.4 V) and solid Li₂S (2.1–2.0 V). Obviously, the Nb₄N₅-Nb₂O₅ heterostructure exhibited a considerably mitigated electrochemical polarization with the highest current intensity and a good overlap of CV profiles (Fig. 3a and Supplementary Fig. 6), indicative of enhanced redox kinetics and sufficient

utilization of the LiPSs along Nb₄N₅-Nb₂O₅ heterostructure³⁵. Moreover, the substantial improvement of the charge transfer from the Nb₄N₅-Nb₂O₅ heterostructure was further verified by electrochemical impedance spectroscopy (EIS). Obviously, the charge-transfer resistance (R_{ct}) of Nb₄N₅-Nb₂O₅ electrode (18.8 Ω) was lower compared with the Nb₄N₅-Nb₂O₅ mix (24.5 Ω), Nb₄N₅ (64.0 Ω) and Nb₂O₅ (111.8 Ω), implying better interfacial kinetics of Nb₄N₅-Nb₂O₅ heterostructure (Fig. 3b)³⁶.

Subsequently, the cyclability was tested at a constant current density of 0.5 C to evaluate the catalytic ability of the cathodes. The initial capacity of the cathode with Nb₄N₅-Nb₂O₅ heterostructure was 1108 mAh g⁻¹, significantly higher than those of Nb₄N₅-Nb₂O₅ mix (1015 mAh g⁻¹), Nb₄N₅ (975 mAh g⁻¹) and Nb₂O₅ (903 mAh g⁻¹) (Fig. 3c and Supplementary Fig. 7). In addition, the cathode with Nb₄N₅-Nb₂O₅ heterostructure showed smaller polarization (150 mV) than those of Nb₄N₅-Nb₂O₅ mix (213 mV), Nb₄N₅ (210mV) and Nb₂O₅ (259 mV) (Supplementary Fig. 8), suggesting the improved redox reaction³⁷. Apart from that, the Nb₄N₅-Nb₂O₅ heterostructure based sulfur cathode retained a high capacity of 1021 mAh g⁻¹ and high Coulombic efficiency \sim 100% over 120 cycles, with an ultralow capacity decay rate of 0.07%. Impressively, a high capacity of 942 mAh g⁻¹ was sustained more than 500 cycles, (Supplementary Fig. 9), which suggested that the shutting effect of LiPSs was significantly suppressed as the strong chemisorption. In contrast, only 760 mAh g⁻¹ for Nb₄N₅-Nb₂O₅ mix (capacity degradation rate of 0.18%), 681 mAh g⁻¹ for Nb₄N₅ (capacity degradation rate of 0.21%), and 443 mAh g⁻¹ for Nb₂O₅ (capacity degradation rate of 0.42%) were remained at 120 cycles (Fig. 3d). The rate performances from 0.5 C to 10 C were further tested to evaluate the superior kinetics of LiPSs conversion. As shown in Fig. 3e, the Nb₄N₅-Nb₂O₅ heterostructure based sulfur cathode presented superior rate response and exceptional reversibility compared with those of the reference electrodes. Specifically, when cycled at step current rates (0.5, 1, 2, 3, 5 and 8 C), such a heterostructure electrode could deliver discharge capacities of 1159, 1095, 1063, 1028, 968 and 899 mAh g⁻¹ with nearly 100% Coulombic efficiency, respectively. Even increasing high current rate to 10 C, an excellent reversible capacity (844 mAh g⁻¹) was remained. In contrast, the batteries employing Nb₄N₅-Nb₂O₅ mix, bare Nb₄N₅ and Nb₂O₅ showed much inferior capacities of 675, 225 and 141 mAh g⁻¹ under the rate of 10 C (Supplementary Fig. 10). Remarkably, the ultrahigh rate capability coupled with ultralow capacity decay rate, has been rarely reported in the former heterostructure materials-based Li-S batteries (Supplementary Table S2), such as MoN-VN (636 mAh g⁻¹ at 2 C with 0.06% decay rate)³⁸, VO₂-VN (587 mAh g⁻¹ at 5 C with 0.06% decay rate)²⁴ and TiO₂-Ni₃S₂ (534 mAh g⁻¹ at 5 C with 0.04% decay rate)³². In addition, the maximum power density (12010 W kg⁻¹) and energy density (1628 Wh kg⁻¹) calculated by the whole mass of cathode are competitive to majority recent reports (Supplementary Fig. 11), such as VN-S (3058W kg⁻¹, 1014 Wh kg⁻¹)³⁹, TiS₂-S (3058 W kg⁻¹, 1014 Wh kg⁻¹)⁴⁰ and ZnS-S (3863 W kg⁻¹, 1396 Wh kg⁻¹)⁴¹.

Lithium Dendrite Suppression of Nb₄N₅-Nb₂O₅ Heterostructure. In fact, the performance of Li-S batteries is severely limited by both unacceptable Li dendrite formation and unstable solid electrolyte

interphase (SEI)⁴². In particular, the uneven Li-ion flux during the repeating plating/stripping is regarded as the main reason causing the safety risks and short lifetime of Li metal anode⁴³. Our 2D Nb₄N₅-Nb₂O₅ heterostructure with dominating hole (1.7–3.5 nm) (Fig. 4a and Supplementary Fig. 12) is expected to benefit the Li-ion redistributor for improving the uniformity of Li-ion flux (Fig. 4b). Besides, the abundant and homogeneously distributed N and O element on the Nb₄N₅-Nb₂O₅ surface can be regarded as lithiophilic sites (binding energy with Li atom: -3.5 eV for Nb₂O₅ and - 5.3 eV for Nb₄N₅) to guide the uniform Li nucleation (Supplementary Fig. 13 and Supplementary Fig. 14)⁴⁴. Half-cell configurations paired with Li foil as counter electrode were developed firstly to explore the reversibility of Nb₄N₅-Nb₂O₅ electrodes. For comparison, the bare Cu electrode was also assembled. After pre-cycling between 0.01-1 V for 4 cycles to stabilize the SEI film and clean impurity (Supplementary Fig. 15)⁴⁵, the Nb₄N₅-Nb₂O₅ showed significantly improved Coulombic efficiency of 99.9% with a steady voltage hysteresis (~ 53 mV) for 300 cycles than the bare Cu foil electrode (58.6% for 16 cycles) at 0.5 mA cm⁻² for tripping/plating capacity of 0.5 mAh cm⁻² (Fig. 4c and Supplementary Fig. 16). Impressively, ultralong cycling lifespan of 1400 h coupled with high average Coulombic efficiency of 99.7% was enabled at 0.5 mA cm⁻² without dendrite growth (Supplementary Fig. 17). In addition, the voltage dropped sharply to -174 mV (vs. Li⁺/Li) at the Li nucleation stage on Cu foil electrode, while the voltage curve of Nb₄N₅-Nb₂O₅ electrode exhibited much smoother voltage dip with a smaller nucleation overpotential of only 56 mV (Fig. 4d). The results indicated the high lithiophilic property of the Nb₄N₅-Nb₂O₅ surface⁴⁶. Then, the long cycling stability of Nb₄N₅-Nb₂O₅ electrode was evaluated by the Li||Li symmetrical configuration. With the pre-stored capacity of 1 mAh cm⁻² at 1 mA cm⁻², excellent cycling stability (1000 h) with highly stable overpotential (~ 10.5 mV) was highlighted for Nb₄N₅-Nb₂O₅/Li||Nb₄N₅-Nb₂O₅/Li symmetric batteries. However, a limited cycle lifespan with obvious fluctuant overpotential (162 mV for 102 h) was observed for the Cu-Li||Cu-Li symmetric batteries (Fig. 4e, f). Even at high current density of 3 mA cm⁻² and large plating capacity of 3 mAh cm⁻², the Nb₄N₅-Nb₂O₅/Li based anode could also exhibit long cycling life more than 900 h with a stable voltage hysteresis of ~ 11.0 mV (Fig. 4g and Supplementary Fig. 18). SEM characterizations were conducted to clearly elucidate the Li deposition morphology after cycling. For the Cu/Li electrode, the cavities and islands were formed on the surface after Li plating and stripping at 1 mA cm⁻² (Supplementary Fig. 19). As for the Nb₄N₅-Nb₂O₅/Li anode, no obvious “dead Li” and Li dendrite were observed after cycling (Fig. 4h and Supplementary Fig. 20), indicative of the homogeneous Li deposition, due to the uniform distribution of Li ions by the holey and lithiophilic Nb₄N₅-Nb₂O₅ nanosheets.

Discussion

Lithium Dendrite Suppression of Nb₄N₅-Nb₂O₅ Heterostructure. Based on the great advantages of Nb₄N₅-Nb₂O₅ heterostructure for both S cathode and Li anode, the as-developed Nb₄N₅-Nb₂O₅/Li (with an excess Li of 50%) and Nb₄N₅-Nb₂O₅/S were paired for full-battery configuration (Nb₄N₅-Nb₂O₅/Li||Nb₄N₅-Nb₂O₅/S) (Fig. 5a). Impressively, a much-improved rate performance was realized with a high discharged

capacity (1163 mAh g^{-1}) and well-maintained two-plateau profiles at 3 C (nearly 87% capacity retention ratio of the capacity at 0.3 C, 1348 mAh g^{-1}) (Fig. 5b, c), suggesting the fast reaction kinetics in the obtained full batteries. The $\text{Nb}_4\text{N}_5\text{-Nb}_2\text{O}_5/\text{Li}||\text{Nb}_4\text{N}_5\text{-Nb}_2\text{O}_5/\text{S}$ full battery could deliver a stable cycling capacity of 856 mAh g^{-1} under the sulfur loading of 5.4 mg cm^{-2} at 0.3 C (Supplementary Fig. 21). Moreover, a high sulfur loading (6.9 mg cm^{-2}), corresponding to N/P (2.4:1) and E/S ($5.1 \mu\text{l mg}^{-1}$), respectively, was successfully assembled. As indicated in Fig. 5d, a practicable areal capacity (5.0 mAh cm^{-2}) with nearly 100% Coulombic efficiency was attained for 200 cycles, which exceeded the common Li-ion batteries (4 mAh cm^{-2}). In addition, a favorable capacity of 1354 mAh g^{-1} could be achieved with excellent cycle stability for 120 cycles for the $\text{Nb}_4\text{N}_5\text{-Nb}_2\text{O}_5/\text{Li}||\text{Nb}_4\text{N}_5\text{-Nb}_2\text{O}_5/\text{S}$ at an elevated temperature of $50 \text{ }^\circ\text{C}$ (Fig. 5e), demonstrative of high temperature affordability. Encouragingly, the assembled $\text{Nb}_4\text{N}_5\text{-Nb}_2\text{O}_5/\text{Li}||\text{Nb}_4\text{N}_5\text{-Nb}_2\text{O}_5/\text{S}$ batteries could keep yellow LED constantly lit for 2 h (Supplementary Fig. 22), highlighting the potential value in practical application. In addition, in situ and in operando XRD showed the efficient conversion of S_8 into short chained solid product Li_2S during the transition to low voltage and *vice versa* (Fig. 5f). Which further indicated that the $\text{Nb}_4\text{N}_5\text{-Nb}_2\text{O}_5$ heterostructure facilitated efficient electron transfer and promoted the Li_2S nucleation and dissolution during cycling, which ensured the minimization of LiPSs shuttle. Most importantly, the full batteries showed an exceptionally low fading rate of only 0.025% during 1000 cycles with high maintaining capacity of 1136 mAh g^{-2} (Fig. 5g and Supplementary Fig. 23). Also, our assembled batteries were superior to a majority of the most advanced Li-S full batteries (Supplementary Table S3), such as mesoporous carbon (6.9 mg cm^{-2} , 607 mAh g^{-1} at 1C, 0.125% decay rate)⁴⁸, TiN-VN (5.6 mg cm^{-2} , 650 mAh g^{-1} at 5C, 0.051% decay rate)²¹ and graphite foam (2.6 mg cm^{-2} , 950 mAh g^{-1} at 3C, 0.057% decay rate)⁴⁹. Overall, the great advantage of our full battery showcases the potential of 2D $\text{Nb}_4\text{N}_5\text{-Nb}_2\text{O}_5$ heterostructure for advanced energy storage equipment in the future.

In summary, a long-cycling, high capacity, and superior rate Li-S full battery was developed by adopting 2D holey $\text{Nb}_4\text{N}_5\text{-Nb}_2\text{O}_5$ heterostructure as difunctional host for shuttling-inhibited sulfur cathode and dendrite-suppressed Li anode. The jointed merits of strong anchoring (Nb_2O_5) and electronic conducting (Nb_4N_5) efficiently complete the immobilization-diffusion-conversion of LiPSs, hence successfully suppressing the LiPSs shuttling and facilitating their reaction kinetics. In addition, remarkably reduced effective deposition current density and evenly dispersed Li-ion flux were realized by the lithiophilic $\text{Nb}_4\text{N}_5\text{-Nb}_2\text{O}_5$ ion redistributor. As a result, the constructed $\text{Nb}_4\text{N}_5\text{-Nb}_2\text{O}_5/\text{Li}||\text{Nb}_4\text{N}_5\text{-Nb}_2\text{O}_5/\text{S}$ batteries showed impressive electrochemical performance including an excellent capacity retention with ultralow capacity fading rate of 0.025% for 1000 cycles and a remarkable area capacity of 5.0 mAh cm^{-2} at high sulfur loading up to 6.9 mg cm^{-1} and low E/S of $5.1 \mu\text{l mg}^{-1}$. The present study provides new perspectives for the design of heterojunction materials for the next-generation practical high energy density Li-S batteries.

Declarations

Data availability

The authors declare that all the data supporting the findings of this study are available within the article and its Supplementary Information or from the corresponding author upon reasonable request.

Competing financial interests:

The authors declare no competing financial interests

Publisher's note

Springer Nature remains neutral with regard to jurisdictional claims in published maps and institutional affiliations

Author contributions

Z.-S. W. conceptualized the idea; H.S., J.Q., and C.D. carried out the experimental work; P. L. did the DFT calculation; H.S., P.D., J.W., L.Z., and Z.-S. W. participated in discussion of the data and preparation of the manuscript. All authors discussed the results and commented on the manuscript. All authors have given approval to the final version of the manuscript.

Acknowledgements

The authors acknowledge financially supported by the National Key R@D Program of China (Grants 2016YBF0100100, and 2016YFA0200200), National Natural Science Foundation of China (Grants 51872283, 21805273, 22005298, 22005297, and 22075279), Liaoning BaiQianWan Talents Program, LiaoNing Revitalization Talents Program (Grant XLYC1807153), Natural Science Foundation of Liaoning Province, Joint Research Fund Liaoning-Shenyang National Laboratory for Materials Science (Grant 20180510038), DICP (DICP ZZBS201708, DICP ZZBS201802, and DICP I202032), DICP&QIBEBT (Grant DICP&QIBEBT UN201702), Dalian National Laboratory For Clean Energy (DNL), CAS, DNL Cooperation Fund, CAS (DNL180310, DNL180308, DNL201912, and DNL201915).

References

1. Kang, K., Meng, Y. S., Bréger, J., Grey, C. P. & Ceder, G. Electrodes with high power and high capacity for rechargeable lithium batteries. *Science* **311**, 977-980 (2006).
2. Peng, Z. Q., Freunberger, S. A., Chen, Y. H. & Bruce, P. G. A reversible and higher-rate Li-O₂ battery. *Science* **337**, 563-566 (2012).
3. Cao, R., Xu, W., Lv, D., Xiao, J. & Zhang, J. G. Anodes for rechargeable lithium-sulfur batteries. *Adv. Energy Mater.* **5**, 1402273 (2015).
4. Bhargav, A., He, J., Gupta, A. & Manthiram, A. Lithium-sulfur batteries: attaining the critical metrics. *Joule* **4**, 285-291 (2020).

5. Tao, Y. *et al.* Kinetically-enhanced polysulfide redox reactions by Nb₂O₅ nanocrystals for high-rate lithium-sulfur battery. *Energy Environ. Sci.* **9**, 3230-3239 (2016).
6. Zhou, G. M. *et al.* Catalytic oxidation of Li₂S on the surface of metal sulfides for Li-S batteries. *P Natl Acad Sci USA* **114**, 840-845 (2017).
7. Zhou, J. *et al.* Deciphering the modulation essence of p bands in Co-based compounds on Li-S chemistry. *Joule* **2**, 2681-2693 (2018).
8. Sun, Z. *et al.* Conductive porous vanadium nitride/graphene composite as chemical anchor of polysulfides for lithium-sulfur batteries. *Nat. Commun.* **8**, 1 (2017).
9. Fu, A. *et al.* Recent advances in hollow porous carbon materials for lithium-sulfur batteries. *Small* **15**, 1804786 (2019).
10. Yang, H. *et al.* Alkali-metal sulfide as cathodes toward safe and high-capacity metal (M= Li, Na, K) sulfur batteries. *Adv. Energy Mater.* **10**, 2001764 (2020).
11. Zhou, L., Danilov, D. L., Eichel, R. A. & Notten, P. H. Host materials anchoring polysulfides in Li-S batteries reviewed. *Adv. Energy Mater.* 2001304 (2020).
12. Zhang, Z. W., Peng, H. J., Zhao, M. & Huang, J. Q. Heterogeneous/homogeneous mediators for high-energy-density lithium-sulfur batteries: progress and prospects. *Adv. Funct. Mater.* **28**, 1707536 (2018).
13. Zhu, B. *et al.* Poly(dimethylsiloxane) thin film as a stable interfacial layer for high-performance lithium-metal battery anodes. *Adv. Mater.* **29**, 1603755 (2017).
14. Qian J. *et al.* High rate and stable cycling of lithium metal anode. *Nat. Commun.* **6**, 6362 (2015).
15. Zhang, Y. *et al.* High-capacity, low-tortuosity, and channel-guided lithium metal anode. *Proc. Natl. Acad. Sci. U. S. A.* **114**, 3584-3589 (2017).
16. Cheng, X. B. *et al.* A review of solid electrolyte interphases on lithium metal anode. *Adv. Sci.* **3**, 1500213 (2016).
17. Shi, H. *et al.* A two-dimensional mesoporous polypyrrole-graphene oxide heterostructure as a dual-functional ion redistributor for dendrite-free lithium metal anodes. *Angew. Chem. Int. Ed.* **59**, 12147-12153 (2020).
18. Yan, K. *et al.* Selective deposition and stable encapsulation of lithium through heterogeneous seeded growth. *Nat. Energy* **1**, 16010 (2016).
19. Zhang, R. *et al.* Coralloid carbon fiber-based composite lithium anode for robust lithium metal batteries. *Joule* **2**, 764-777 (2018).
20. Liu, Y. Y. *et al.* Lithium-coated polymeric matrix as a minimum volume-change and dendrite-free lithium metal anode. *Nat. Commun.* **7**, 10992 (2016)..
21. Yao, Y. *et al.* A dual-functional conductive framework embedded with TiN-VN heterostructures for highly efficient polysulfide and lithium regulation toward stable Li-S full batteries. *Adv. Mater.* **32**, 1905658 (2019).

22. Moorthy, B., Kim, J.-H., Lee, H.-W. & Kim, D. K. Vertically aligned carbon nanotubular structure for guiding uniform lithium deposition via capillary pressure as stable metallic lithium anodes. *Energy Storage Mater.* **24**, 602-609 (2020).
23. Ye, H. *et al.* Stable Li plating/stripping electrochemistry realized by a hybrid Li reservoir in spherical carbon granules with 3D conducting skeletons. *J. Am. Chem. Soc.* **139**, 5916-5922 (2017).
24. Song, Y. *et al.* Synchronous immobilization and conversion of polysulfides on a VO₂-VN binary host targeting high sulfur load Li-S batteries. *Energy Environ. Sci.* **11**, 2620-2630 (2018).
25. Zhou, T. *et al.* Twinborn TiO₂-TiN heterostructures enabling smooth trapping-diffusion-conversion of polysulfides towards ultralong life lithium-sulfur batteries. *Energy Environ. Sci.* **10**, 1694-1703 (2017).
26. Tao, Y. *et al.* Kinetically-enhanced polysulfide redox reactions by Nb₂O₅ nanocrystals for high-rate lithium-sulfur battery. *Energy Environ. Sci.* **9**, 3230-3239 (2016).
27. Ge, W. *et al.* Conductive cobalt doped niobium nitride porous spheres as an efficient polysulfide convertor for advanced lithium-sulfur batteries. *J. Mater. Chem. A* **8**, 6276-6282 (2020).
28. Cui, H. *et al.* Niobium nitride Nb₄N₅ as a new high-performance electrode material for supercapacitors. *Adv. Sci.* **2**, 1500126 (2015).
29. Yin, L.-C. *et al.* Understanding the interactions between lithium polysulfides and N-doped graphene using density functional theory calculations. *Nano Energy* **25**, 203-210 (2016).
30. Li, S. *et al.* Improve redox activity and cycling stability of the lithium-sulfur batteries via in situ formation of a sponge-like separator modification layer. *Int J Energ Res.* **44**, 4933-4943 (2020).
31. Li, B. Q. *et al.* Expediting redox kinetics of sulfur species by atomic-scale electrocatalysts in lithium-sulfur batteries. *InfoMat* **1**, 533-541 (2019).
32. Wang, R. *et al.* Bidirectional catalysts for liquid-solid redox conversion in lithium-sulfur batteries. *Adv. Sci.* **32**, 2000315 (2020).
33. Xu, Z. L. *et al.* Exceptional catalytic effects of black phosphorus quantum dots in shuttling-free lithium sulfur batteries. *Nat. Commun.* **9**, 4164 (2018).
34. Luo, D. *et al.* Revealing the rapid electrocatalytic behavior of ultrafine amorphous defective Nb₂O_{5-x} nanocluster toward superior Li-S performance. *ACS Nano* **14**, 4849-4860 (2020).
35. Liu, D. *et al.* Catalytic effects in lithium-sulfur batteries: promoted sulfur transformation and reduced shuttle effect. *Adv. Sci.* **5**, 1700270 (2018).
36. Yang, X. *et al.* Promoting the transformation of Li₂S₂ to Li₂S: significantly increasing utilization of active materials for high-sulfur-loading Li-S batteries. *Adv. Mater.* **31**, 1901220 (2019).
37. Tsao, Y. *et al.* Designing a quinone-based redox mediator to facilitate Li₂S oxidation in Li-S batteries. *Joule* **3**, 872-884 (2019).
38. Ye, C. *et al.* 2D MoN-VN heterostructure to regulate polysulfides for highly efficient lithium-sulfur batteries. *Angew. Chem. Int. Ed.* **57**, 16703-16707 (2018).

39. He, J. & Manthiram, A. Long-life, high-rate lithium-sulfur cells with a carbon-free VN host as an efficient polysulfide adsorbent and lithium dendrite inhibitor. *Adv. Energy Mater.* **10**, 1903241 (2020).
40. Huang, X. *et al.* Sandwich-like ultrathin TiS₂ nanosheets confined within N, S codoped porous carbon as an effective polysulfide promoter in lithium-sulfur batteries. *Adv. Energy Mater.* **9**, 1901872 (2019).
41. Xu, J. *et al.* Promoting lithium polysulfide/sulfide redox kinetics by the catalyzing of zinc sulfide for high performance lithium-sulfur battery. *Nano Energy* **51**, 73-82 (2018).
42. Jin, Y. *et al.* Self-healing SEI enables full-cell cycling of a silicon-majority anode with a coulombic efficiency exceeding 99.9%. *Energy Environ. Sci.* **10**, 580-592 (2017).
43. Shen, X. *et al.* The failure of solid electrolyte interphase on Li metal anode: structural uniformity or mechanical strength? *Adv. Energy Mater.* **10**, 1903645 (2020).
44. Chen, X. *et al.* Lithiophilicity chemistry of heteroatom-doped carbon to guide uniform lithium nucleation in lithium metal anodes. *Sci. Adv.* **5**, eaau7728 (2019).
45. Liu, S. *et al.* Crumpled graphene balls stabilized dendrite-free lithium metal anodes. *Joule* **2**, 184-193 (2018).
46. Zhang, R. *et al.* Lithiophilic sites in doped graphene guide uniform lithium nucleation for dendrite-free lithium metal anodes. *Angew. Chem. Int. Ed.* **56**, 7764-7768 (2017)..
47. Yang, X., Li, X., Adair, K., Zhang, H. & Sun, X. Structural design of lithium-sulfur batteries: from fundamental research to practical application. *Electrochem. Energy Rev.* **1**, 239-293 (2018).
48. Cao, D. *et al.* Stable lithium-sulfur full cells enabled by dual functional and interconnected mesocarbon arrays. *J. Mater. Chem. A* **7**, 3289-3297 (2019).
49. Jin, S. *et al.* Covalently connected carbon nanostructures for current collectors in both the cathode and anode of Li-S batteries. *Adv. Mater.* **28**, 9094-9102 (2016).

Figures

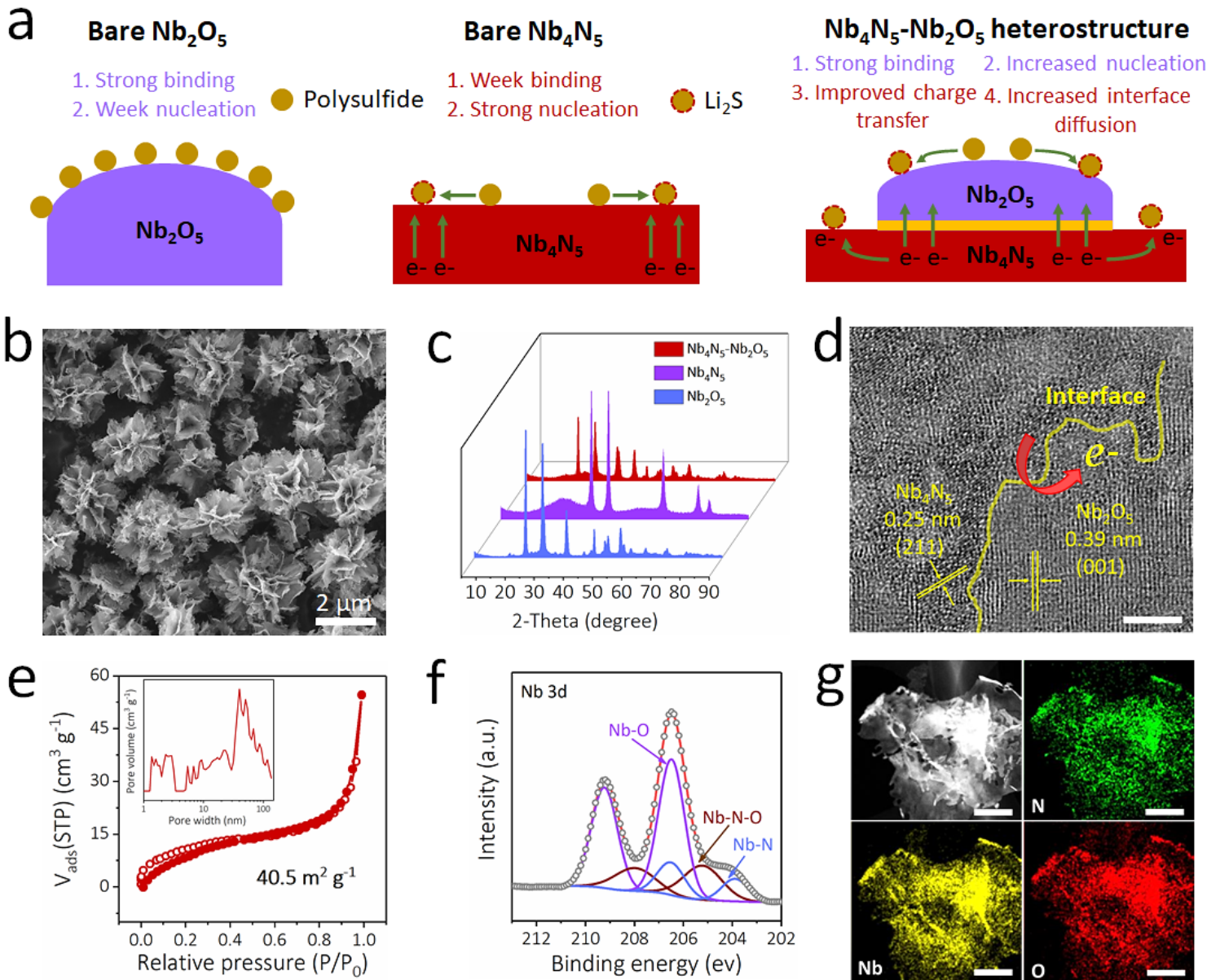


Figure 1

Schematics of the catalytic mechanism and characterization of Nb₄N₅-Nb₂O₅ Heterostructure. (a) Schematic illustration of the polysulfides anchoring-diffusion-conversion processes on bare 2D Nb₂O₅, bare 2D Nb₄N₅ and 2D Nb₄N₅-Nb₂O₅ heterostructure surface. (b) SEM image of Nb₄N₅-Nb₂O₅ heterostructures. (c) XRD patterns of Nb₂O₅, Nb₄N₅ and Nb₄N₅-Nb₂O₅ heterostructure. (d) HRTEM image and (e) nitrogen adsorption-desorption isotherm of Nb₄N₅-Nb₂O₅ heterostructure. Inset is its pore size distribution. (f) High-resolution XPS Nb 3d spectrum of Nb₄N₅-Nb₂O₅ heterostructure. (g) HAADF-STEM image of Nb₄N₅-Nb₂O₅ heterostructure and corresponding element mapping of N, Nb, and O element. Scale bars: (b) 2 μm, (d) 5 μm, and (g) 300 nm

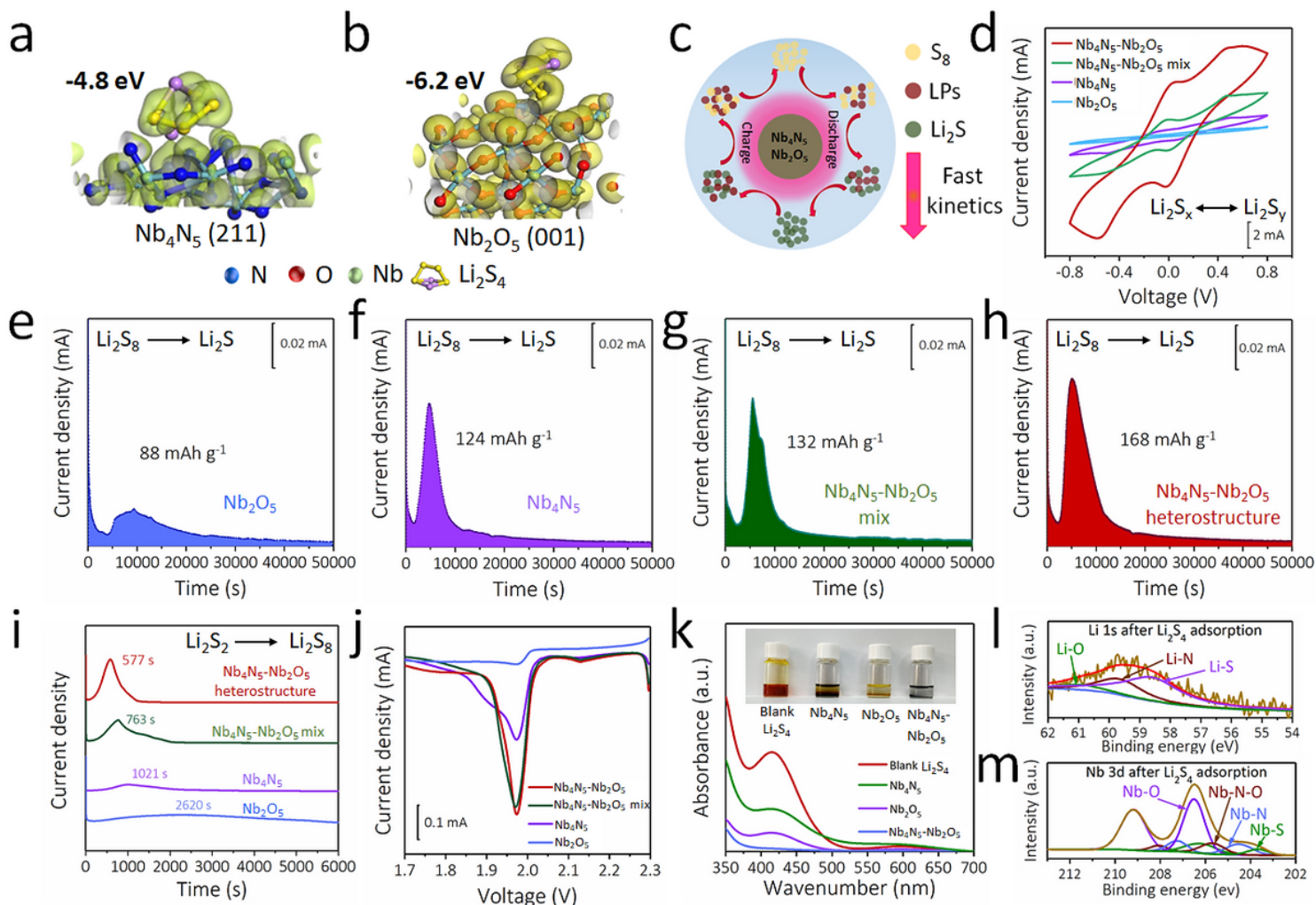


Figure 2

Electrocatalytic and adsorption effects of Nb₄N₅-Nb₂O₅ heterostructure. (a, b) Optimized geometries and their corresponding binding energies of Li₂S₄ on (a) Nb₄N₅ (211) and (b) Nb₂O₅ (001) surfaces. (c) Schematic illustration of the reaction pathways of the sulfur cathode catalyzed by Nb₄N₅-Nb₂O₅ heterostructure. (d) CV curves of Li₂S₆ symmetric batteries employing Nb₄N₅-Nb₂O₅ heterostructure, Nb₄N₅-Nb₂O₅ mix, Nb₄N₅, or Nb₂O₅ electrodes obtained at 5 mV s⁻¹. (e-h) Potentiostatic discharge curves of Li₂S₈ electrolyte discharged at 2.05 V on the (e) Nb₂O₅, (f) Nb₄N₅, (g) Nb₄N₅-Nb₂O₅ mix, and (h) Nb₄N₅-Nb₂O₅ heterostructure, respectively. (i) Potentiostatic charge profiles at 2.40 V on Nb₄N₅-Nb₂O₅ heterostructure, Nb₄N₅-Nb₂O₅ mix, Nb₄N₅, and Nb₂O₅ electrodes to evaluate the dissolution behaviors of Li₂S₂. (j) LSV analyses of Nb₄N₅-Nb₂O₅ heterostructure, Nb₄N₅-Nb₂O₅ mix, Nb₄N₅, and Nb₂O₅ electrodes with Li₂S₄ catholyte. (k) UV-Vis spectra of Li₂S₄ with variation in color upon adsorption by blank Li₂S₄ solution, Nb₄N₅, Nb₂O₅, and Nb₄N₅-Nb₂O₅ heterostructure. (l, m) High-resolution XPS (l) Li 1s and (m) Nb 3d spectra of Nb₄N₅-Nb₂O₅ heterostructure after adsorption of Li₂S₄.

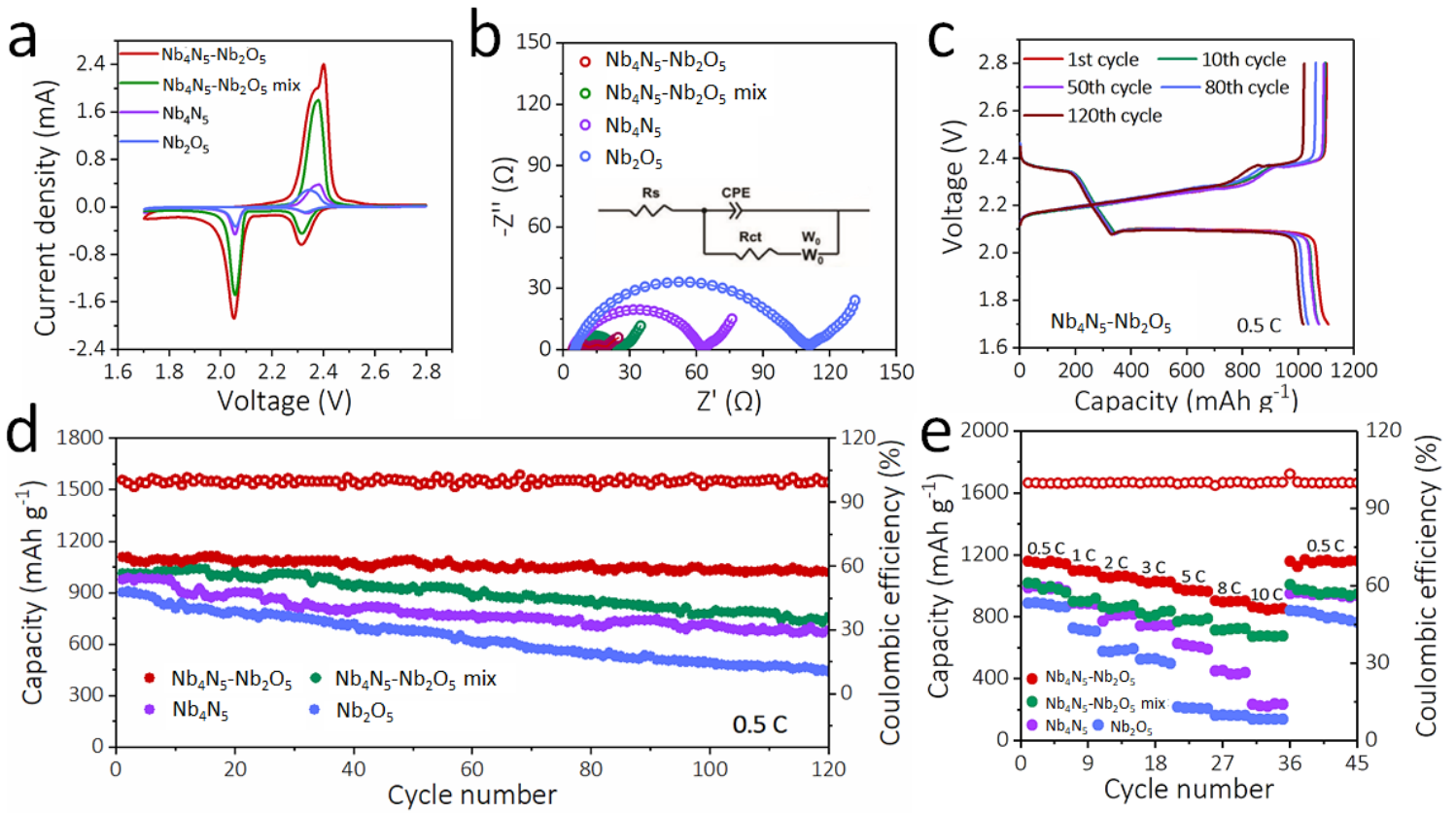


Figure 3

The electrochemical performance of Li-S battery based on Nb₄N₅-Nb₂O₅ Cathode. (a) CV curves of Li-S batteries using Nb₄N₅-Nb₂O₅ heterostructure, Nb₄N₅-Nb₂O₅ mix, Nb₄N₅, and Nb₂O₅ electrodes as the sulfur hosts obtained at a scan rate of 1 mV s⁻¹. (b) Nyquist plots of Li-S batteries with different cathodes before cycling. (c) Galvanostatic charge and discharge profiles of Li-S batteries with Nb₄N₅-Nb₂O₅ cthode at 0.5 C. (d) Cycling performance of Li-S batteries with Nb₄N₅-Nb₂O₅ heterostructure, Nb₄N₅-Nb₂O₅ mix, Nb₄N₅, and Nb₂O₅ electrodes at 0.5 C. (e) Rate performance of Li-S batteries with different cathodes.

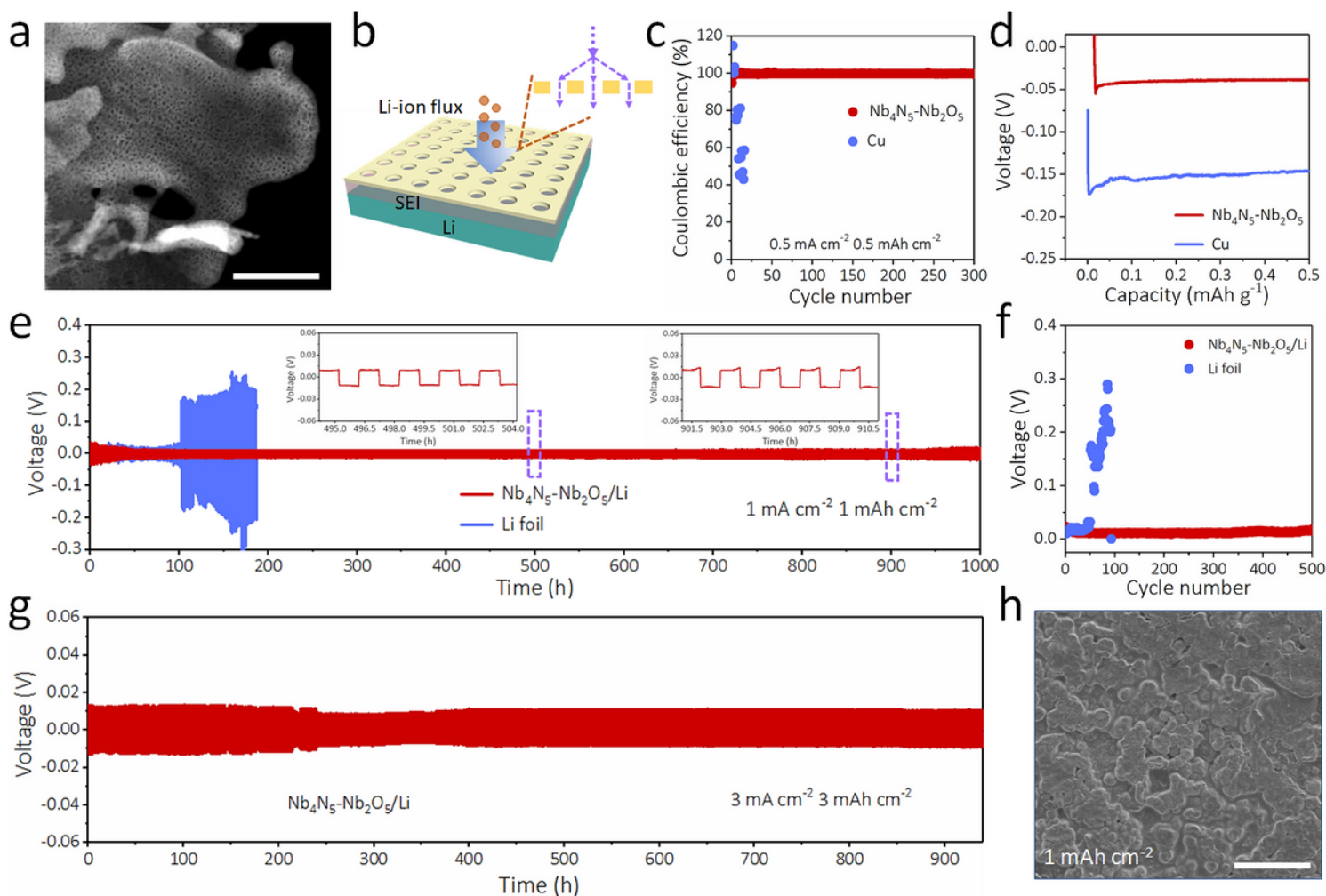


Figure 4

Lithium dendrite suppression of Nb₄N₅-Nb₂O₅ heterostructure. (a) High angle annular dark field-scanning transmission electron microscope/microscopy (HAADF-STEM) image of Nb₄N₅-Nb₂O₅ heterostructure. (b) Schematic illustration of the Li-ion redistribution behavior of the holey Nb₄N₅-Nb₂O₅ for dendrite-free Li anode. (c) Coulombic efficiencies and (d) enlarged plating-stripping curves of Nb₄N₅-Nb₂O₅ and Cu foil electrodes at current density of 0.5 mA cm⁻² with the capacity of 0.5 mAh cm⁻². (e) Voltage profiles of the symmetric batteries based on Nb₄N₅-Nb₂O₅/Li and Cu-Li electrodes at current density of 1 mA cm⁻² under stripping/plating capacity of 1 mAh cm⁻², and (f) corresponding voltage hysteresis variation with cycling number. Inset of (e) is the enlarged voltage-time curves at different times. (g) Voltage profile of the symmetric batteries with different electrodes at current density of 3 mA cm⁻² with a capacity of 3 mAh cm⁻². (h) SEM image of Nb₄N₅-Nb₂O₅/Li electrode after cycling. Scale bars: (a) 50 nm, and (h) 50 μm

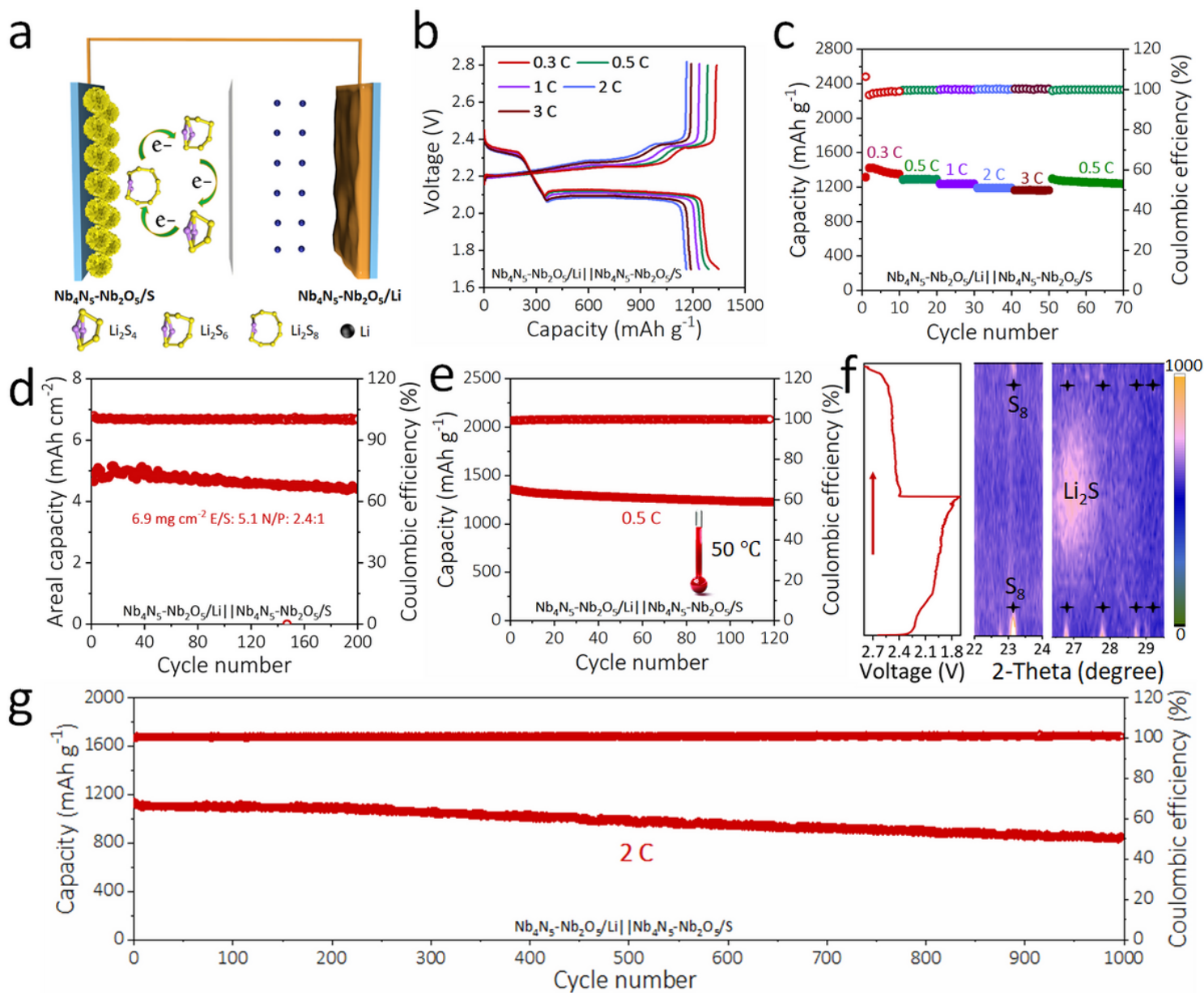


Figure 5

Performance of $\text{Nb}_4\text{N}_5\text{-Nb}_2\text{O}_5/\text{Li}||\text{Nb}_4\text{N}_5\text{-Nb}_2\text{O}_5/\text{S}$ full battery. (a) Schematic configuration of $\text{Nb}_4\text{N}_5\text{-Nb}_2\text{O}_5$ heterostructure based Li-S full batteries. (b) Galvanostatic charge and discharge profiles of $\text{Nb}_4\text{N}_5\text{-Nb}_2\text{O}_5/\text{Li}||\text{Nb}_4\text{N}_5\text{-Nb}_2\text{O}_5/\text{S}$ batteries obtained at various rates. (c) Rate capability of $\text{Nb}_4\text{N}_5\text{-Nb}_2\text{O}_5/\text{Li}||\text{Nb}_4\text{N}_5\text{-Nb}_2\text{O}_5/\text{S}$ full batteries. (d) Areal capacity of $\text{Nb}_4\text{N}_5\text{-Nb}_2\text{O}_5/\text{Li}||\text{Nb}_4\text{N}_5\text{-Nb}_2\text{O}_5/\text{S}$ battery obtained at 0.3 C with high sulfur loading of 6.9 mg cm^{-2} . (e) Cycling performance of the $\text{Nb}_4\text{N}_5\text{-Nb}_2\text{O}_5/\text{Li}||\text{Nb}_4\text{N}_5\text{-Nb}_2\text{O}_5/\text{S}$ full battery operated at an elevated temperature of 50°C . (f) In situ XRD contour plots of the $\text{Nb}_4\text{N}_5\text{-Nb}_2\text{O}_5/\text{Li}||\text{Nb}_4\text{N}_5\text{-Nb}_2\text{O}_5/\text{S}$ cathode with the corresponding discharge-charge curves on the left and the diffraction intensity chart on the right. (g) Long-term cycling stability of 1000 cycles of $\text{Nb}_4\text{N}_5\text{-Nb}_2\text{O}_5/\text{Li}||\text{Nb}_4\text{N}_5\text{-Nb}_2\text{O}_5/\text{S}$ battery measured at 2 C.

Supplementary Files

This is a list of supplementary files associated with this preprint. Click to download.

- [SupportingInformation.docx](#)